13th International Symposium on Particle Image Velocimetry – ISPIV 2019
Munich, Germany, July 22-24, 2019

Stereo-PIV Measurements of Vortex-Interaction Effects on Generic Delta Wing Planforms

Stefan Pfnür, Christian Breitsamter

Technical University of Munich, Department of Mechanical Engineering, Chair of Aerodynamics and Fluid Mechanics, Garching, Germany

stefan.pfnuer@tum.de

Abstract

Low aspect ratio configurations with leading-edge vortex dominated flow exhibit typical flight mechanics instabilities like a pitch-up or a roll reversal at medium to high angles of attack. Those are linked to the bursting of leading-edge vortices. An approach that might be able to tackle these instabilities is the intended triggering of multiple, interacting leading-edge vortices. Therefore, the system of interacting leading-edge vortices on a double delta wing and a triple delta wing configuration was investigated by means of stereo particle image velocimetry measurements at asymmetric free stream conditions. Cross-flow sections were measured on the windward and leeward wing sides to obtain comprehensive information about the asymmetric flow structures. Both configurations indicate a system of an inboard leading-edge vortex and a midboard leading-edge vortex at each wing side. The inboard leading-edge vortex develops at a highly swept or a a medium swept wing section for the double or the triple delta wing configuration, respectively. The fully-developed vortex systems at the leeward wing side and the vortex system exhibiting vortex bursting at the windward wing side show significant differences between both configurations. The characteristics of the vortex interaction are dominated by the state of the inboard leading-edge vortex and thus, by the properties of the inboard wing section. As a result, the triple delta wing features a more upstream and less abrupt vortex breakdown due to the reduced wing sweep of the inboard wing section and the associated vortex interaction.

1 Introduction

High-agile aircraft configurations typically feature wings of low aspect ratio and medium to high leading-edge sweep. Such wings exhibit a vortex dominated flow field at both wing sides. The leading-edge vortices enable the exploitation of favorable non-linear lift characteristics. There have been extensive investigations on the characteristics of leading-edge vortices, which develop at slender and non-slender wings. The leading-edge vortices are already observable at low angles of attack. As the angle of attack increases, the leading-edge vortices become unstable and start to burst in consequence of an arising adverse pressure gradient towards the wing trailing edge. Wings with a high leading-edge sweep of $\varphi > 60^\circ$ are subject to a vortex breakdown associated with an abrupt and significant divergence of the vortex cross section, a reverse core flow and strong velocity fluctuations in the vortex core, cf. Breitsamter (2008); Gursul (2005, 2004). The position of the flow reversal in the vortex core is defined as the breakdown location for this type of leading-edge vortex.

As the leading-edge sweep decreases, the vortex breakdown is observed at lower angles of attack. At non-slender and semi-slender wings with a leading-edge sweep of $50^\circ < \varphi < 60^\circ$ there is also a change in the vortex breakdown characteristics, see Gursul et al. (2005). The vortex breakdown is less abrupt and begins with the transition from a jet-type to a wake-type axial core flow over a certain region. The flow reversal of the axial core flow does not necessarily occur. Compared to the vortex breakdown at slender wings, the expansion of the vortex core is less abrupt. This makes it more difficult to clearly define the vortex breakdown location, see Gursul et al. (2005). For sideslip conditions, the vortex breakdown becomes asymmetric with a more upstream breakdown location at the windward wing side than at the leeward wing side, see Hummel et al. (1984). Longitudinal, lateral and directional flight mechanics instabilities like a pitch-up, roll-reversal, and directional divergence result from the leading-edge vortex breakdown characteristics. The aformentioned instabilities have been observed for generic low-aspect ratio wing-body configurations by

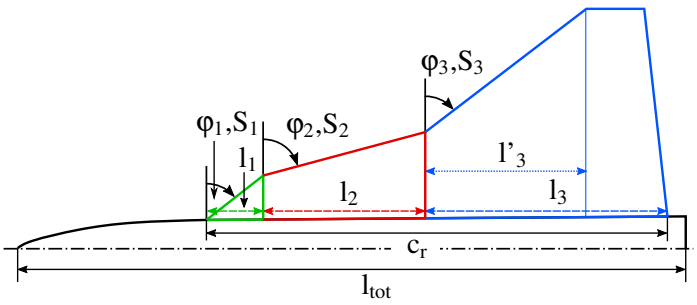

(a) Planform sketch NA1 W1

(b) NA1 W1 W/T model in the test section

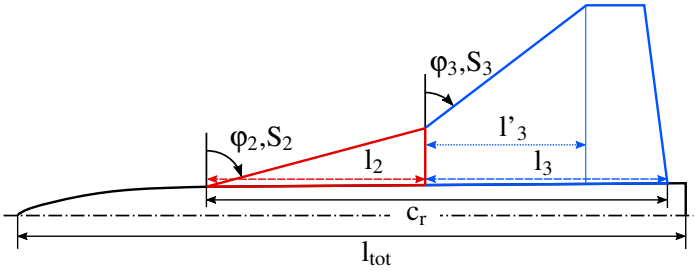

(c) Planform sketch NA1 W2

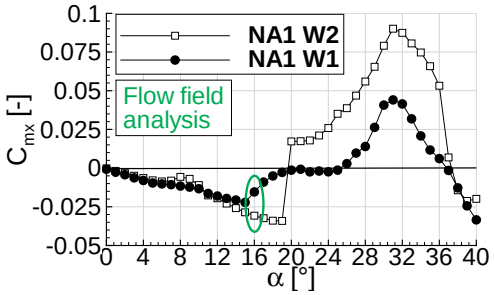

(d) Rolling moment coefficient at $\beta = 5°$

Figure 1: Wing planforms, wind tunnel model, and rolling moment at selected free stream conditions.

e.g. Hummel et al. (1984) and for several types of high-performance aircraft, cf. Chambers and Anglin (1969); Greer (1972); John and Kraus (1978); Staudacher et al. (1978).

Different measures can be found in the literature aiming at alleviating or eliminating the occurring instabilities for high-agile aircraft configurations. Geometric variations of details of such configurations have been investigated. These include the position and size of the vertical tails, see Greer (1972); Hummel and Brümmer (1994), the application of leading-edge/vortex flaps, see Greer (1972), the modification of the strake, cf. Ward and Erb (1986), or (fore)body geometry variations, see Brandon et al. (1986) and modifications, cf. Hummel et al. (1984); Rao et al. (1987); Tristrant et al. (1996); Hitzel and Osterhuber (2017). All measures aim at the stabilization of the leading-edge vortex and consequently the shift of the vortex breakdown to higher angles of attack.

Another approach to tackle the instabilities is the intended triggering of the development of multiple, interacting leading-edge vortices. The development of multiple leading-edge vortices is determined by the corresponding wing planform. The spatial proximity of the leading-edge vortices results in their interaction, which has an influence on the vortex characteristics and consequently, on the global aerodynamic characteristics. The interaction is intended to be provoked in a way that entails a stabilizing effect on the vortex system and thus, improves the global flight mechanics stability and control. The flow physics of the interacting leading-edge vortices needs to be well known to be able to evaluate the potential of the approach. Detailed flow field analyses are therefore necessary. Stereo particle image velocimetry (Stereo-PIV) measurements are an appropriate method to obtain detailed information on the vortex-dominated flow field of low aspect ratio configurations. In the study at hand, the flow field of a low aspect ratio wing fuselage configuration with multiple swept wings is investigated at asymmetric free stream conditions by means of Stereo-PIV measurements.

Table 1: Geometrical parameters of the configurations NA1 W1 and NA1 W2.

			NA1 W1	**NA1 W2**
c_r	root chord	$[m]$	0.802	0.802
s	half span	$[m]$	0.417	0.367
S_{ref}	reference area	$[m^2]$	0.329	0.266
AR	aspect ratio	$[-]$	2.11	2.03
λ	taper ratio	$[-]$	0.15	0.16
l_{tot}	model length	$[m]$	1.16	1.16
l_μ	mean aerodynamic chord	$[m]$	0.468	0.426
l_1/c_r	relative length, wing section 1	$[-]$	0.125	-
l_2/c_r	relative length, wing section 2	$[-]$	0.35	0.475
l_3'/c_r	relative length, wing section 3'	$[-]$	0.35	0.35
l_3/c_r	relative length, wing section 3	$[-]$	0.475	0.475
φ_1	sweep, wing section 1	$[deg]$	52.5	-
φ_2	sweep, wing section 2	$[deg]$	75	75
φ_3	sweep, wing section 3	$[deg]$	52.5	52.5

2 Experimental Technique

2.1 Wind Tunnel Model, Test Facility, and Test Conditions

The investigated geometry is a generic low-aspect-ratio wing-fuselage configuration. The investigated model is subject to a common research program in cooperation with Airbus Defence and Space (Airbus DS) and the German Aerospace Center (DLR). Furthermore, it is embedded in the NATO AVT-316 task group called "Vortex Interaction Effects Relevant to Military Air Vehicle Performance". The wing of the configuration is designed as a flat plate with sharp leading edges. The model can be equipped with wings of different planform. The so-called NA1 W1 configuration is a triple delta wing configuration with three different consecutive wing sections featuring a varying leading-edge sweep, see Fig. 1(a). The so-called NA1 W2 configuration is a double delta wing configuration with two different consecutive wing sections of varying leading-edge sweeps, see Fig. 1(c). Detailed information on the geometric parameters of both configurations is summarized in Tab. 1. Due to the sharp wing leading edges, trip dots were only attached to the fuselage nose to force turbulent boundary-layer characteristics. This ensures the comparability of the experimental data to numerical results obtained by (unsteady) Reynolds-averaged Navier-Stokes simulations associated with fully-turbulent boundary layers. The wind tunnel model was attached via a rear sting to a three-axis support, which allows for the adjustment of the angles of attack and sideslip, see Fig. 1(b). Parts of the left fuselage side, parts of the left upper wing surface and the left leading edge of the wind tunnel model were painted black to reduce the laser light reflections observed by the cameras. The experiments were carried out in the Göttingen-type low-speed wind tunnel (W/T) A of the Chair of Aerodynamics and Fluid Mechanics of the Technical University of Munich (TUM-AER). The W/T was operated with an open test section which has a size of $1.8 \times 2.4 \times 4.8\,m^3$ (height $\times$ width $\times$ length). The experiments were performed at low subsonic speeds with a Reynolds number of $Re = 3 \cdot 10^6$ based on the reference length $l_{Re} = 1\,m$ and a Mach number of $Ma = 0.15$. The presented results were obtained for an angle of attack of $\alpha = 16^\circ$ and an angle of sideslip of $\beta = 5^\circ$. The corresponding rolling moment coefficients C_{mx} of both configurations for $\beta = 5^\circ$ are shown in Fig. 1(d). For positive angles of sideslip, negative values indicate a stable behavior in roll with a right wing up motion. Positive values indicate an unstable behavior with a right wing down motion. Both configurations are close to their maximum lateral stability for the selected free stream condition of $\alpha = 16^\circ$, $\beta = 5^\circ$.

2.2 Stereo Particle Image Velocimetry

A Stereo-PIV measurement system was used to measure the flow field above the wing in several cross-flow sections. The Stereo-PIV system was mounted on a three-axis traversing system next to the W/T test section, see Fig. 2(a). The traversing system itself can be rotated around its vertical axis. Furthermore, the cameras

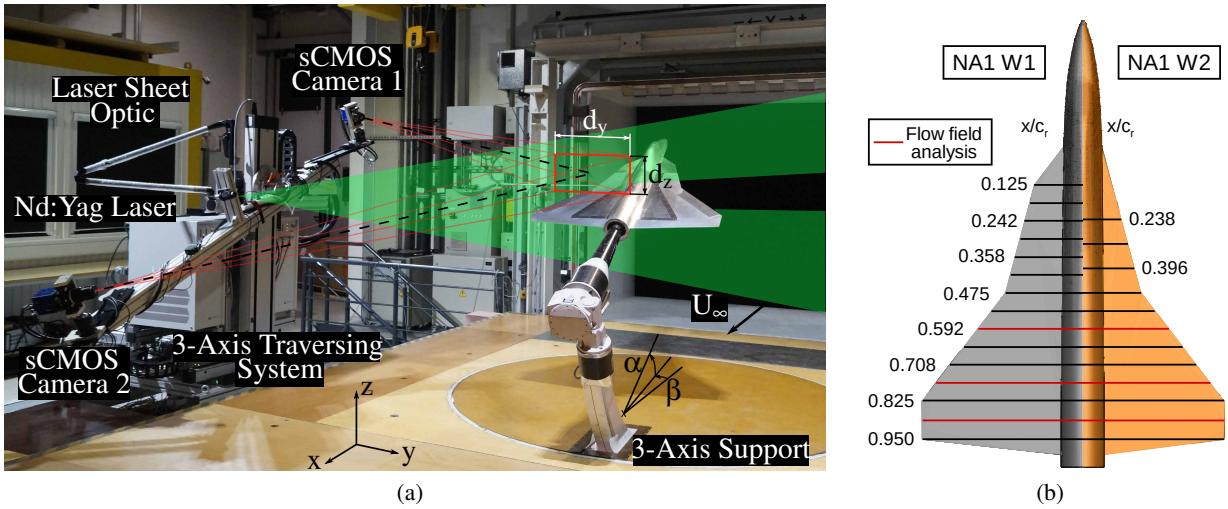

(a) (b)

Figure 2: (a) Stereo-PIV measurement setup and (b) measured cross-flow sections.

Table 2: Stereo-PIV setup and processing parameters.

Angle between cameras	$\Theta = 60^\circ$
Image pairs per section	$N = 400$
Final field of view	$d_y \times d_z \approx 0.45 \times 0.210\,m^2$
Number of vectors per section	≈ 45000
Spatial resolution	$\Delta d = 1.49 \cdot 10^{-3}\,m$
Non-dimensional spatial resolution	$\Delta d/s = 3.58 \cdot 10^{-3}, 4.07 \cdot 10^{-3}$
Software package	LaVision DaVis 8
Main algorithm	Stereo cross-correlation
Iteration options	Multi-pass, decreasing size
Initial interrogation window	64×64 pixel, 0% overlap, 1 pass
Final interrogation window	32×32 pixel, 50% overlap, 3 passes

and the laser sheet can be rotated around the traversing system's lateral axis. These two adjustments enable the alignment of the cameras and the laser sheet with the angle of attack and the angle of sideslip of the W/T model. A double pulsed Nd:Yag laser with a maximum power of $325\,mJ$ per pulse and a wave length of $532\,nm$ illuminated the measurement plane. Two sCMOS cameras with a resolution of 2560×2160 pixel were placed up- and downstream of the measurement plane. The cameras were equipped with NIKON lenses with a focal length of $135\,mm$. The sCMOS sensor planes were tilted by Scheimpflugadapters to meet the Scheimpflug criterion, cf. Raffel et al. (2007). Seeding particles with a diameter of $d_{part} \approx 1\,\mu m$ were fed into the flow. The cameras recorded 400 image pairs per cross-flow section with a sampling frequency of $f_{meas} = 15\,Hz$. The presented quantities in this study are the mean values determined from the 400 accquired samples. Information on the applied Stereo-PIV setup, the vector-calculation parameters, and the resulting field of view is summarized in Tab. 2. The maximum uncertainties of the absolute velocities were quantified to $|V_{err}/U_\infty| \approx 0.084$, see Sciacchitano and Wieneke (2016). The maximum uncertainties were observed in the vortex centers of the strongly interacting vortices. The majority of the flow field including the shear layers and rotational cores of the vortices provide uncertainties of $|V_{err}/U_\infty| < 0.015$. The measured cross-flow sections are perpendicular to the body-fixed longitudinal axis of the W/T model. A number of 13 to 15 sections was measured within the range of $0.125 \leq x/c_r \leq 0.95$, see Fig. 2(b). The flow field is discussed at the windward and leeward wing sides in the highlighted cross-flow sections. The measurement setup only allows for measurements on the left wing side. The data that is presented at the right wing side for $\beta = 5^\circ$ was actually measured at the left wing side for $\beta = -5^\circ$. The obtained vector fields were mirrored to the right wing side for the discussion of the results.

3 Flow-Field Analysis

The flow field is analyzed for the NA1 W1 and NA1 W2 configurations in the three selected cross-flow sections $x/c_r = \{0.592, 0.767, 0.877\}$, see the highlighted cross-flow sections in Fig. 2(b). The discussion comprises the non-dimensional velocity components and the non-dimensional axial vorticity.

3.1 The NA1 W2 Configuration

Figure 3 illustrates the non-dimensional axial velocity u/U_∞ and the non-dimensional axial vorticity $\omega_x l_\mu / U_\infty$ at the three selected cross-flow sections of the NA1 W2 configuration. The figures showing the non-dimensional axial velocity also include every fourth in-plane velocity vector representing the cross-flow velocities. The flow field is depicted at both wing sides. The right wing side represents the windward wing side, whereas the left wing side represents the leeward wing side.

Figures 3(a) and 3(b) show the flow field of the most upstream selected cross-flow section at $x/c_r = 0.592$. Two leading-edge vortices at each wing side can be noticed from the $\omega_x l_\mu / U_\infty$ field. At each wing side, the more inboard leading-edge vortex is the so-called inboard vortex (IBV) developing at the slender inboard wing section of the NA1 W2 configuration. For the left and right wing side, the IBV is called left inboard vortex (LIBV) and right inboard vortex (RIBV), respectively. The more outside positioned leading-edge vortices have their origin at the kink from the highly swept wing section to the medium swept wing section at $x/c_r = 0.475$, see Fig. 2(b). They are called left or right midboard vortex (LMBV/RMBV) for the left or right wing side, respectively. There is a fifth vortex observable by an area of positive axial vorticity at the upper left fuselage side. This is the vortex originating from the fuselage/canopy and it is called the fuselage vortex (FLV). The rotation orientation of the FLV indicates its development on the right fuselage side (RFLV). Due to the positive angle of sideslip, the RFLV moves from the right fuselage side to the left fuselage side.

It can be recognized that the RIBV and the LIBV are disconnected from the wing leading-edges and the RMBV and the LMBV are connected to the shear layer shed at the leading edge. The angle of sideslip of $\beta = 5^\circ$ also makes for a difference in the lateral position of the leading-edge vortices. The RIBV is located more inboard at $y/s \approx 0.345$ compared to the LIBV located at $y/s \approx -0.4$. The difference in the MBVs' lateral locations is not that significant, since they have developed only at a distance $\Delta x/c_r = 0.142$ upstream of the considered cross-flow section.

The IBVs and the MBVs exhibit a jet-type axial core flow, see Fig. 3(a). The areas of maximum flow velocity are separated, whereas an overall accelerated flow between the IBVs and MBVs is present. The axial velocity in the IBVs is $u/U_\infty \approx 2.5$ and therefore higher than the axial velocities in the MBVs. There, the axial velocity is $u/U_\infty \approx 2$. It is also observed that the axial velocity in the vortices at the windward side is slightly higher than at the leeward side. The velocity vectors show the high cross-flow velocities induced by the leading-edge vortices. High lateral velocities in outboard direction are induced at the wing surfaces by the vortex systems.

A strong interaction of the RIBV with the RMBV and the LIBV with the LMBV is present in the cross-flow section at $x/c_r = 0.767$, see Figs. 3(c) and 3(d). The axial velocity fields at both wing sides do not show clearly separated areas of highly accelerated velocities for the IBVs and the MBVs. At each wing side, there is an increased area showing velocities of $u/U_\infty \approx 2$. In these areas there are each two peaks of high axial velocity of $u/U_\infty \approx 2.5$, representing the IBVs and the MBVs. Compared to the more upstream section at $x/c_r = 0.592$, the IBVs axial velocities are at a similar level as the axial velocities of the IBVs. The acceleration of the axial core flow of the LMBV and the RMBV is likely to be an effect of the IBV-MBV interaction.

The axial vorticity distribution highlights the vortex systems on both sides, showing the LIBV and the LMBV on the leeward side and the RIBV and the RMBV on the windward side. At the left wing side, a distinct rotation of the LIBV and the LMBV around each other is recognized. Due to the co-rotation of both vortices, the LMBV is deflected upwards and inwards around the LIBV. The LIBV is deflected towards the wing surface and in outboard direction. Although the LMBV is significantly moved away from the leading edge, it is still connected to the shear layer shed at the leading edge. Consequently, the vortex system is still fed with vorticity.

The right wing side depicts a similar picture. The RIBV and the RMBV are rotating in anti-clockwise direction around each other. Differences in comparison to the left wing side can be seen in the exact locations of the RIBV and the RMBV. The larger distance between the RIBV and the RMBV observed at $x/c_r = 0.592$ results in a weaker vortex interaction compared to the left wing side. The induced cross-flow velocities of the RIBV and the RMBV on one another are directly dependent on the distance between the two vortices.

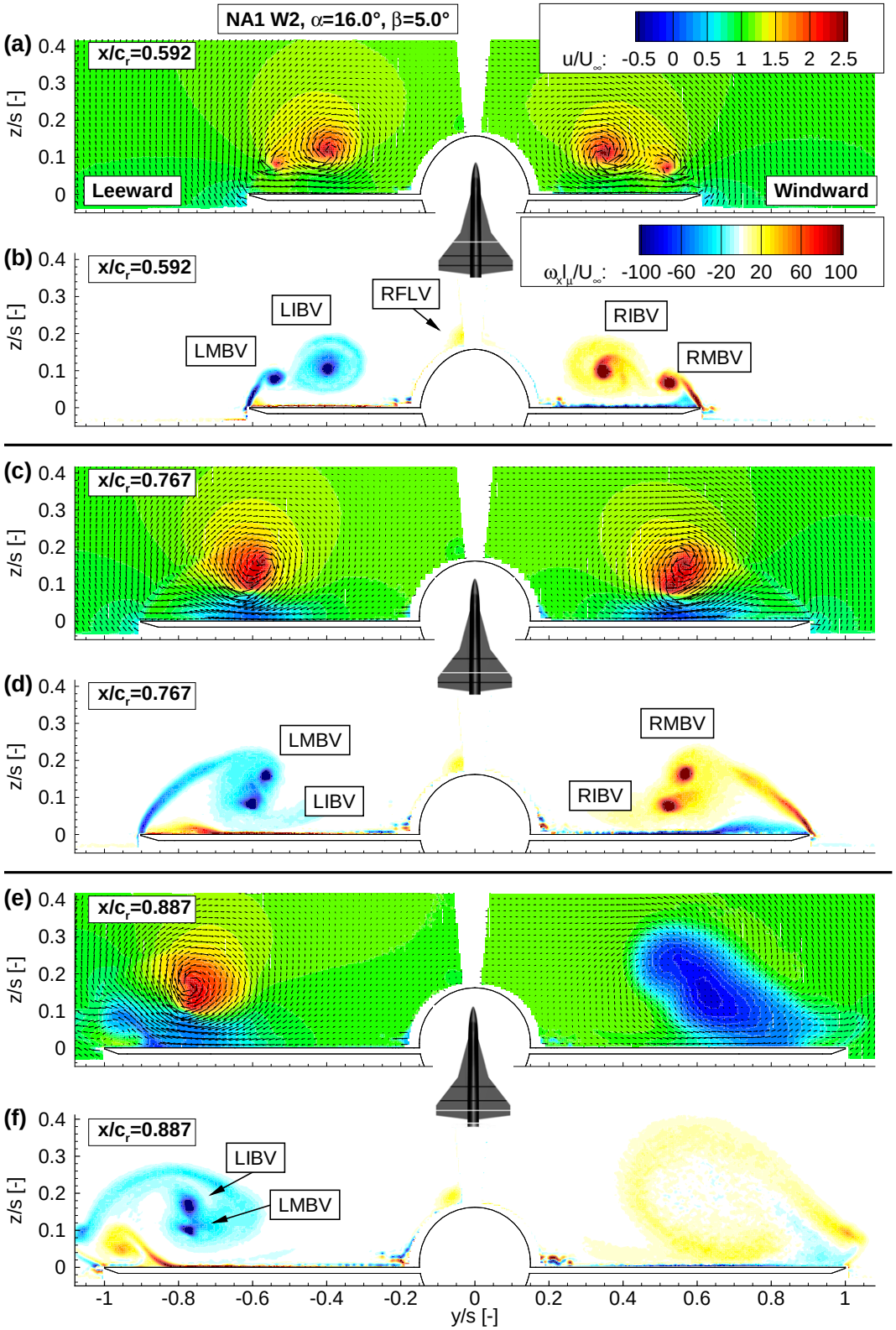

Figure 3: a,c,e) Non-dimensional axial velocity and b,d,f) non-dimensional axial vorticity sections of the NA1 W2 configuration at $\alpha = 16°$ and $\beta = 5°$.

A larger distance results in a weaker interaction with otherwise similar vortex properties. Consequently, a less progressed rotation of the RIBV and the RMBV around each other is noticed.

The area of significantly reduced axial velocity, which is located between the vortex system and the wing surface on both wing sides is actually not a flow deceleration. The velocity magnitude near the wing surface reads $V_{abs}/U_\infty \approx 2$. It is an effect of the velocities being shown in the body-fixed coordinate system. The vortex axes of the LIBV and the RIBV are strongly deflected in outboard direction because of the strong interaction with their associated MBVs. The velocities induced by the outwards deflected IBVs in the vicinity of the wing surface are consequently observed as reduced axial velocities in the body-fixed coordinate system.

The most downstream section at $x/c_r = 0.887$ shows significant differences between both wing sides, see Fig. 3(e) and 3(f). At the left wing side, the system of the LIBV and the LMBV is still existent. The rotation of the two vortices has further progressed and there is still the jet-type axial core flow present. The LIBV and the MIBV are now at the similar span-wise location, with the LIBV being above the LMBV. The two vortices are still enclosed by the leading-edge shear layer. Between the leading edge and the vortex system, the boundary-layer flow separates and rolls up showing a weak anti-clockwise rotation. The separating boundary layer shows a reverse flow, whereas the area of local $\omega_x l_\mu/U_\infty$-maximum at $y/s \approx -0.96$ and $z/s \approx 0.05$ exhibits a positive axial velocity. At the right wing side in contrast, the vortex system is broken down and a large area of reverse flow is present. The breakdown occurs abruptly and affects the complete vortex system. A strong divergence of the vortex core and an almost zero axial vorticity level is noticed in the wake-type flow.

The flow field shows consistent characteristics with the existent lateral stability at this free stream condition, cf. Fig. 1(d). The leading-edge vortices typically induce higher suction levels at the windward side as long as they are fully developed. The vortex bursting near the wing trailing edge has no adverse effect on the lateral stability yet, since only a minor area of the wing is affected. However, the vortex bursting onset at the windward side will move upstream with an increasing angle of attack, which will result in a roll reversal, cf. Fig. 1(d).

3.2 The NA1 W1 Configuration

The NA1 W1 configuration is equipped with a triple delta wing, see Fig. 1(a). The IBVs develop, in contrast to the NA1 W2 configuration, at the non-slender inboard wing sections. As described earlier, leading-edge vortices developing at wings with a medium leading-edge sweep burst more upstream and show different vortex bursting characteristics. The characteristics of the vortex systems developing at the NA1 W1 configuration are discussed by the non-dimensional axial velocity u/U_∞ and the non-dimensional axial vorticity $\omega_x l_\mu/U_\infty$ at the three selected cross-flow sections, see Fig. 4.

The NA1 W1 configuration shows a comparable vortex system as the NA1 W2 configuration, cf. Fig. 4 and Fig. 3. At $x/c_r = 0.592$, both wing sides show a vortex system consisting of the LIBV and LMBV and the RIBV and the RMBV on the left and right wing sides, see Fig. 4(a) and 4(b). The IBVs develop at the non-slender inboard wing sections and the MBVs develop at the kink from the highly swept to the medium swept wing section at $x/c_r = 0.475$,cf. Fig. 1(a). Both the IBV and the MBV on both wing sides are well represented by the axial vorticity field. At the left wing side, the LIBV and the LMBV exhibit both a jet-type axial core flow and high absolute values in the axial vortitiy. The velocity vectors indicate the high induced cross-flow velocities in the outboard direction near the wing surface. At the right wing side, the RIBV is already burst, which is indicated by the wake-type axial core flow with velocity levels of $u/U_\infty \approx 0.04$. The axial core flow of the burst RIBV is considerably decelerated but no reverse flow is observed. The axial vorticity still indicates significant rotation of the RIBV. The increased area of axial vorticity indicates a slight divergence of the RIBV. The axial vorticity values in the outer area of the rotational core of the vortex, however, are still of similar values as for the fully-developed LIBV. The viscous core of the RIBV, which is represented by a very high axial vorticity, has undergone a significant expansion. This can be identified by an increased area exhibiting medium vorticity levels. The velocity and axial vorticity distributions indicate an effect of the vortex bursting primarily on the viscous core. The rotational core is considerably less affected. The current state of the RIBV can be seen as an intermediate state between a fully-developed and a burst vortex. The velocity vectors also confirm the high induced cross-flow velocities, especially, near the wing surface. The RMBV is, in contrast to the RIBV, stable and shows a jet-type axial core flow.

At $x/c_r = 0.767$ the stable LIBV and the stable LMBV show an ongoing interaction with a clock-wise rotation around each other, see Figs. 4(c) and 4(d). The interaction between the LIBV and the LMBV is comparable with the interaction observed for the NA1 W2 configuration, cf. Figs. 3(c) and 3(d). The rotation of the LIBV and the LMBV around each other at the NA1 W1 configration is less progressed in comparison

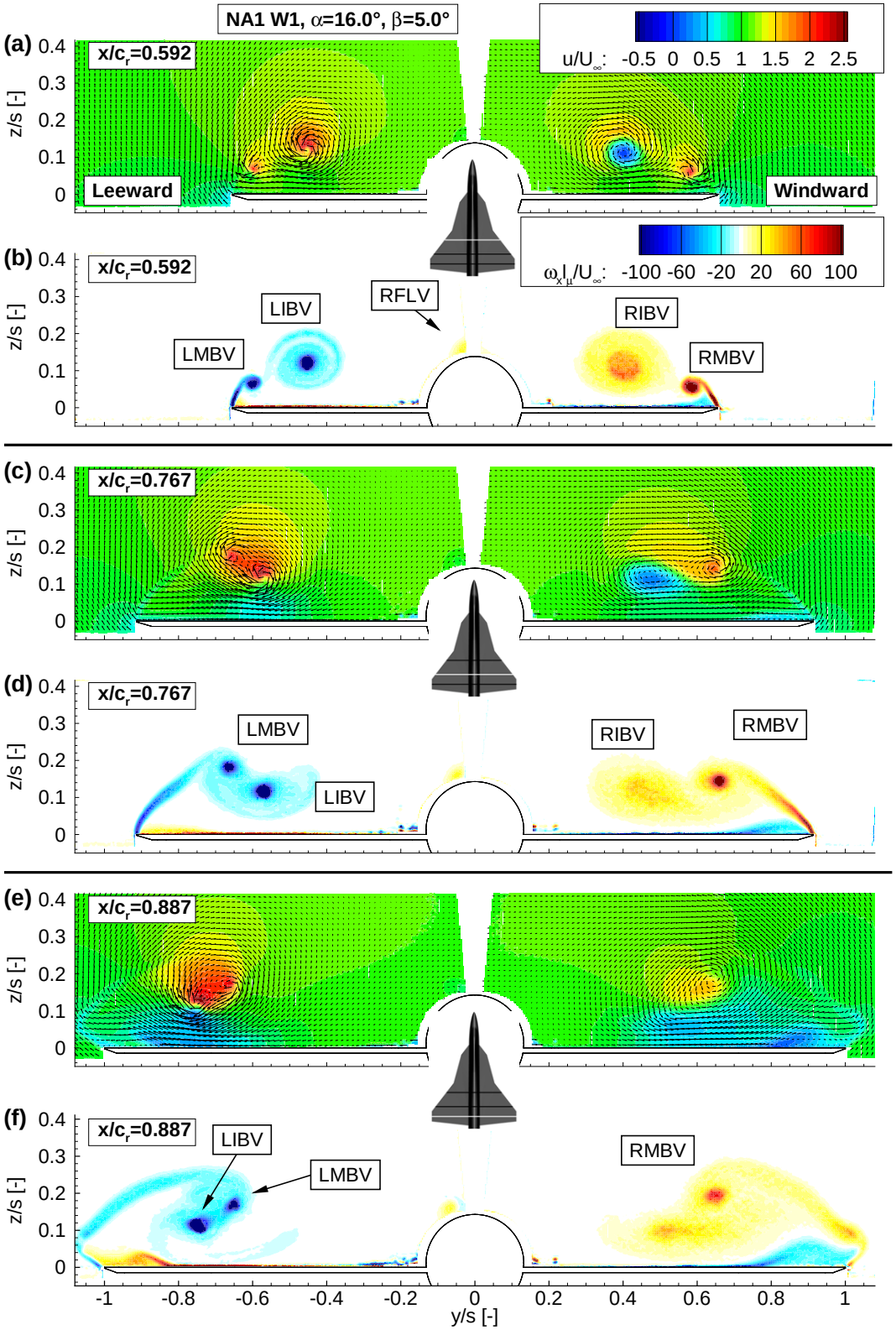

Figure 4: a,c,e) Non-dimensional axial velocity and b,d,f) non-dimensional axial vorticity sections of the NA1 W1 configuration at $\alpha = 16°$ and $\beta = 5°$.

to the same location at the NA1 W2 configuration. This is probably the effect of the location of the LIBV and the LMBV to each other. The vertical distance between the LIBV and the LMBV reads $\Delta z/s \approx 0.055$ for the NA1 W1 configuration and $\Delta z/s \approx 0.028$ for the NA1 W2 configuration. Consequently, the starting point for the vortex interaction is different resulting in a varying vortex trajectory for both configurations.

The RIBVs axial core flow has slightly recovered now exhibiting axial velocities of $u/U_\infty \approx 0.24$. The velocity vectors and the area of increased axial vorticity indicate the presence of rotation. There is, however, not a vortex in the original sense present anymore. The RIBV is significantly deformed due to the interaction with the RMBV and there are no high maximum axial vorticity levels observed any more. Nevertheless, the considerable induced cross-flow velocities in outboard direction near the wing surface indicate that there is still a noticeable suction at the wing surface, despite the observed state of the RIBV. The RMBV features a jet-type axial core flow and high axial vorticity levels indicating its stability. However, the axial velocity peak is reduced in comparison to the upstream cross-flow section and compared to the LMBV. The RMBV obviously stabilizes the axial core flow of the RIBV which, however, leads to a reduction of its own axial core flow velocity.

The most downstream cross-flow section at $x/c_r = 0.887$ is illustrated in Figs. 4(e) and 4(f). At the left wing side, the flow patterns are similar to those observed for the NA1 W2 configuration, cf. Figs. 3(e) and 3(f). At the right wing side, the axial velocity of the RIBV wake is further recovered. The axial velocity of the RMBV is in contrast further decreased. At this section, a significant decrease in the axial vorticity of the RMBV can also be noticed. The RMBV is, although no change from jet-type to wake-type axial core flow is observed, in a state between fully developed and burst. The bursting of the RIBV and the RMBV take place in a smooth way and are smeared over a certain axial distance. Although the RIBV and the RMBV are in a kind of an intermediate state between fully developed and burst, there is still a rotation in the velocity field, which also leads to the smooth surface separation of the flow deflected towards the wing leading edge.

Although the windward vortex system is subject to vortex bursting, the combination of the wing planform and the vortex-vortex interaction results in smooth and delayed vortex bursting characteristics. According to the stable behavior in roll, cf. Fig. 1(d), the near-wall cross-flow velocities at the upper wing side induced by the vortex system still result in significant suction levels. The breakdown of the windward vortex system is already affecting the rolling moment, however, the upcoming roll-reversal onset is smooth, as it can be expected from the observed vortex breakdown characteristics.

4 Conclusion

Stereo-PIV measurements of the interacting leading-edge vortices of a double and a triple delta wing configuration were performed at low subsonic, asymmetric free stream conditions. Both configurations exhibit a system of two interacting leading-edge vortices at each wing side. The inboard vortex develops on a slender or a non-slender wing section for the double or the triple delta wing configuration, respectively. The midboard vortex develops for both configurations at a non-slender wing section. The properties of the inboard wing section determine the state of the inboard vortex at the beginning of the interaction with the midboard vortex. Therefore, the inboard vortex is the dominating factor for the differences observed in the vortex interaction characteristics in the presented study. The interaction between the two vortices is noticed in the deflection of the vortex axes. The co-rotating vortices rotate around each other. The progression of that rotation is, inter alia, dependent on the relative location of the interacting vortices to each other at the beginning of the interaction. A larger distance between the vortices results in a weaker rotation. Furthermore, the axial velocities of the interacting vortices are affected by one another. The asymmetric free stream condition results in a different effective leading-edge sweep at both wing sides and consequently to an unequal flow field. Both configurations exhibit a vortex bursting on the windward wing side. The leading-edge bursting at the double delta wing shows the abrupt divergence of the vortex cross-section and a large area with reverse flow. The vortex bursting affects the complete vortex system. The triple delta wing configuration shows a completely different behavior. The vortex bursting appears much more upstream and is smeared over a large axial distance. It shows retarded flow but no reversed flow and affects primarily the inboard vortex. Furthermore, the wake of the bursting inboard vortex exhibits considerable rotation, which still induces suction at the upper wing side.

In a next step, the turbulent characteristics of the burst vortex system will be investigated. The vortex interaction itself taking place for both configurations and, especially, the alleviated abruptness of the breakdown at the triple delta wing configuration, are likely to be associated with considerable different turbulence levels and dominant frequencies than observed for leading-edge vortices at classical delta wings.

Acknowledgements

The support of this investigation by the German Research Association (DFG, grant BR 1511/13-1) is gratefully acknowledged. Moreover, the fruitful cooperation with Airbus Defence and Space is much obliged. The authors also highly appreciate the assistance during the wind tunnel tests by Dominik Sedlacek.

References

Brandon JM, Murri DG, and Nguyen LT (1986) Experimental study of effects of forebody geometry on high angle of attack static and dynamic stability and control. in *15th Congress of the International Council of the Aeronautical Sciences*. ICAS Paper 5.4.1

Breitsamter C (2008) Unsteady Flow Phenomena Associated with Leading-Edge Vortices. *Progress in Aerospace Sciences* 44:48–65

Chambers JR and Anglin EL (1969) Analysis of lateral-directional stability characteristics of a twin-jet fighter airplane at high angles of attack. NASA-TN-D-5361

Greer HD (1972) Summary of directional divergence characteristics of several high-performance aircraft configurations. NASA-TN-D-6993

Gursul I (2004) Recent Developments in Delta Wing Aerodynamics. *The Aeronautical Journal* 108:437–452

Gursul I (2005) Review of Unsteady Vortex Flows over Slender Delta Wings. *Journal of Aircraft* 42:299–319

Gursul I, Gordnier R, and Visbal M (2005) Unsteady Aerodynamics of Non-Slender Delta Wings. *Progress in Aerospace Sciences* 41:515–557

Hitzel SM and Osterhuber R (2017) Enhanced Maneuverability of a Delta-Canard Combat Aircraft by Vortex Flow Control. *Journal of Aircraft* 55:1090–1102

Hummel D and Brümmer A (1994) Aerodynamics of a slender wing with vertical fins at low speed. in *19th Congress of the International Council of the Aeronautical Sciences*. ICAS Paper 4.3.4

Hummel D, John H, and Staudacher W (1984) Aerodynamic characteristics of wing-body-combinations at high angles of attack. in *14th Congress of the International Council of the Aeronautical Sciences*. ICAS Paper 2.7.1

John H and Kraus W (1978) High angle of attack characteristics of different fighter configurations. in *Specialists' Meeting on "High Angle of Attack Aerodynamics"*. volume CP-247 of *AGARD Conference Proceedings*. pages 2.1–2.15. AGARD

Raffel M, Willert CE, Wereley ST, and Kompenhans J (2007) *Particle Image Velocimetry*. chapter Stereo PIV, pages 211–212. Springer. 2nd edition

Rao DM, Murri DG, and Moskovitz A (1987) Forebody Vortex Management for Yaw Control at High Angles of Attack. *Journal of Aircraft* 24:248–254

Sciacchitano A and Wieneke B (2016) PIV uncertainty propagation. *Measurement Science and Technology* 27

Staudacher W, Laschka B, Poisson-Quinton P, and Ledy JP (1978) Aerodynamic characteristics of a fighter-type configuration during and beyond stall. in *Specialists' Meeting on "High Angle of Attack Aerodynamics"*. volume CP-247 of *AGARD Conference Proceedings*. pages 8.1–8.15. AGARD

Tristrant D, Renier O, and Farcy D (1996) Flow analysis and control surface evaluation at high angles of attack for enhanced manoeuvrability. in *20th Congress of the International Council of the Aeronautical Sciences*. ICAS Paper 3.1.2

Ward DT and Erb RE (1986) Use of hinged strakes for lateral control at high angles of attack. AIAA Paper 1986-2278